

Frustrated magnetism in Mott insulating $(V_{1-x}Cr_x)_2O_3$

J. C. Leiner,^{1,2,3,*} H. O. Jeschke,^{4,5} R. Valentí,⁵ S. Zhang,⁶ A. T. Savici,³ Jiao Lin,³ M. B. Stone,³ M. D. Lumsden,³ Jiawang Hong,^{7,8} O. Delaire,^{9,8} Wei Bao,¹⁰ and C. L. Broholm^{6,3}

¹Center for Correlated Electron Systems, Institute for Basic Science (IBS), Seoul 08826, Korea

²Department of Physics and Astronomy, Seoul National University, Seoul 08826, Korea

³Neutron Scattering Division, Oak Ridge National Laboratory, Oak Ridge, TN 37831 USA

⁴Research Institute for Interdisciplinary Science, Okayama University, Okayama 700-8530, Japan

⁵Institut für Theoretische Physik, Goethe-Universität Frankfurt,
Max-von-Laue-Straße 1, 60438 Frankfurt am Main, Germany

⁶Institute for Quantum Matter and Department of Physics and Astronomy,
The Johns Hopkins University, Baltimore, Maryland 21218 USA

⁷School of Aerospace Engineering, and Institute of Advanced Structure Technology,
Beijing Institute of Technology, Beijing 100081, China

⁸Materials Science and Technology Division, Oak Ridge National Laboratory, Oak Ridge, TN 37831 USA

⁹Department of Mechanical Engineering and Materials Science and Department of Physics,
Duke University, Durham, North Carolina 27708 USA

¹⁰Department of Physics, Renmin University of China, Beijing 100872, China

(Dated: April 24, 2018)

V_2O_3 famously features all four combinations of paramagnetic versus antiferromagnetic, and metallic versus insulating states of matter in response to %-level doping, pressure in the GPa range, and temperature below 300 K. Using time-of-flight neutron spectroscopy, we have mapped the inelastic magnetic neutron scattering cross section over a wide range of energy and momentum transfer in the chromium stabilized antiferromagnetic and paramagnetic insulating phases (AFI & PI). By fitting the measured excitation spectrum in the AFI phase, we establish a phenomenological exchange Hamiltonian and then show density functional theory (DFT) computations can account for the exchange constants to within the experimental accuracy. We then use DFT and neutron scattering to show the PI phase is a quasi-two-dimensional honeycomb antiferromagnet with competing near and next nearest neighbor exchange interactions ($J_2/J_1 = 0.2$) that place it near a putative spin liquid phase. Treated with a Gaussian approximation, the DFT spin Hamiltonian accounts in detail for the short-range dynamic spin correlations of the PI phase. The magnetic frustration and degeneracy of the PI phase is relieved by the rhombohedral to monoclinic transition at $T_N = 185$ K due to a significant magneto-elastic coupling. This leads to the recognition that magnetic frustration is an inherent property of the paramagnetic phase in $(V_{1-x}Cr_x)_2O_3$ and plays an important role in suppressing the magnetic long range ordering temperature and exposing a large phase space for the Mott metal-insulator transition.

PACS numbers: 71.30.+h, 75.10.Jm, 75.10.Kt, 75.30.Ds, 78.70.Nx

I. INTRODUCTION

Metal to insulator transitions come in many guises, but for transition metal oxides they generally involve magnetic or structural symmetry breaking. V_2O_3 however, offers a singular counter example. As a function of chromium doping, $(V_{1-x}Cr_x)_2O_3$ undergoes a *paramagnetic* metal to insulator transition that is accompanied by a volume expansion but no global magneto-structural symmetry breaking (Fig. 1 (a)) [1–3]. In this paper we identify magnetic frustration in paramagnetic insulating (PI) $(V_{1-x}Cr_x)_2O_3$ as a rare characteristic that contributes to expose the available paramagnetic phase space for the unique Mott metal-insulator transition [4] by suppressing long range magnetic order. We show that, in contrast with the PI phase, the magnetic interactions of the monoclinic antiferromagnetic insulating (AFI) phase

are all simultaneously satisfied in the ordered state. The magneto-structural transition from the PI to the AFI (Fig 1(a)) thus lifts degeneracies associated with frustrated interactions in a spin-Peierls-like transition [5] as in other frustrated magnets such as $ZnCr_2O_4$ [6] and ZnV_2O_4 [7, 8].

Our conclusions are based on a careful examination of magnetic interactions in $(V_{0.96}Cr_{0.04})_2O_3$ through inelastic neutron scattering (INS) and density functional theory (DFT). The low T monoclinic antiferromagnetic insulator has conventional spin-wave excitations that allow us to determine a non-frustrated exchange Hamiltonian by measuring and analyzing the spin wave dispersion relation. This in turn allows us to establish DFT as a reliable method to determine exchange constants in V_2O_3 . We then use DFT to determine the exchange constants in the PI and show, using a Gaussian approximation, that these are consistent with the measured diffuse magnetic neutron scattering. The PI is a strongly frustrated quasi-two-dimensional honeycomb antiferromagnet with a nominal critical temperature below 10 K. That phase

* Corresponding author: jleiner@alumni.nd.edu

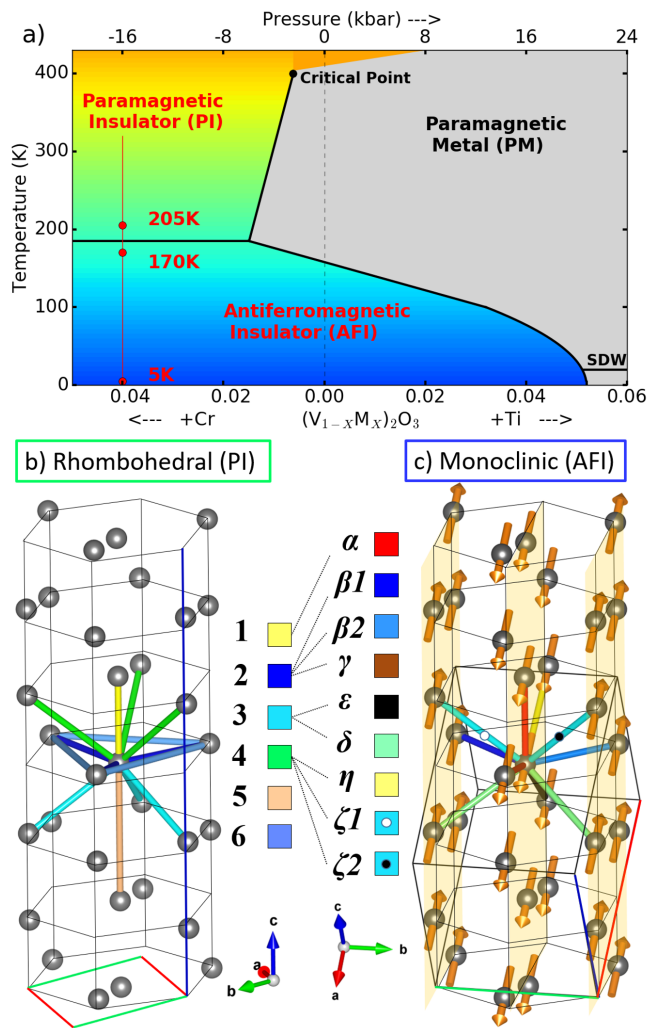


FIG. 1. (a) V_2O_3 phase diagram showing the extent of the AFI, PI, and PM phases [9] as a function of both chemical substitution (bottom axis) and the equivalent applied pressure (top axis). (b) The rhombohedral structure of the PI phase, with the color labeled exchange interactions (1-6) determined in the paper. Black hexagons outline the pseudo-hexagonal (corundum) unit cell. (c) The distorted crystal structure (monoclinic unit cell shown) and magnetic structure in the AFI phase [10], where the magnetic moments are ferromagnetically aligned in monoclinic $a+c$ planes, which are then stacked antiferromagnetically along the monoclinic b axis. Greek indices indicate the updated nearest neighbor bond configuration resulting from the monoclinic distortion. Oxygen atoms have been omitted for clarity.

transition is, however, preempted by the spin-Peierls-like magneto-structural transition at 185 K.

Our observations suggest that the large region of paramagnetism in the phase diagram of V_2O_3 is made possible by magnetic frustration which deeply suppresses magnetic order in the Mott insulator. This reinforces the importance of exploring metallization of frustrated magnets through doping [11, 12] and pressure [13–15].

A. Summary of prior work on V_2O_3

While our work reveals a previously unappreciated aspect of V_2O_3 , it is by no means the first effort to understand spin interactions in this material [9, 16–23]. In a comprehensive work in 1978, Castellani *et al.* [24] invoked the formation of vanadium dimers and e_g orbital order to explain the measured antiferromagnetic (AFM) structure [10] in the AFI phase. Many other theoretical studies of V_2O_3 used simpler one-orbital models which neglect the orbital degrees of freedom and assume the same kind of AFM correlations for all phases of V_2O_3 [25]. In 1993, a different kind of AFM order was found in the metallic phase of $V_{2-y}O_3$ [26, 27] stabilized to low temperatures through vanadium deficiency. It was further shown through INS that the phase transition to the AFI phase, from either the metallic or the insulating paramagnetic phases, abruptly shifts the critical magnetic wave vector from (10ℓ) to $(\frac{1}{2}\frac{1}{2}0)$ [28, 29]. This is inconsistent with predictions from one-orbital theories, and indicates the transition is not a conventional order-to-disorder type of magnetic transition. This behavior seemed to be naturally explained within the coupled spin-orbital model of Rice *et al.* [30], as an orbital ordering transition with accompanying antiferromagnetism. The symmetric $SU(4)$ spin-orbital model has since attracted considerable theoretical interest [31–33].

Subsequent resonant x-ray scattering experiments discovered a new type of Bragg peak [34], which was explained as the order parameter of the e_g orbital ordering [35, 36]. Polarization-dependent x-ray absorption spectroscopy (XAS) measurements [37] reached the unexpected conclusion that there is an $S = 1$ state at each V site, with dominant orbital occupation in e_g^π and a small admixture of the a_{1g} orbital. This was supported by LDA+U [38] and LDA+DMFT [39, 40] calculations with selected values for the Hubbard and the Hund’s coupling energies. In the last years, fully charge self-consistent LDA+DMFT calculations [1, 41, 42] and ARPES measurements [43] however, indicate a much weaker orbital polarization that may influence the nature of the metal-to-insulator transition (MIT). Recently, the role of defect-induced local symmetry breakings upon doping in $(V_{1-x}Cr_x)_2O_3$ has been highlighted as an important ingredient to understand the MIT [4].

Regarding the PI to AFI transition, the initial LDA+U [38] calculations for the insulating phase showed the magnetic structure has a drastic effect on the electronic band structure. The calculated magnetic structures, determined without orbital degeneracy or orbital ordering being necessary, were found to be consistent with experiments. Alternatively, an $S = 1$ model with orbital degeneracy was suggested [44–46] in which stable magnetic and orbital structures were systematically analyzed and anomalous features of the AFI transition were qualitatively explained. In this picture, the phase transition from PI to AFI was interpreted as being a fundamentally a structural and orbital occupational ordering transition

[47] that brings the spin system deeply into a long range ordered state without the usual critical regime associated with a growing spin correlation length.

B. Outline

In view of the ongoing debate on the origin of the insulating phases in V_2O_3 , it is important to provide an experimental anchor with reliable values of magnetic exchange interactions that limit the parameter space of $S = 1$ theories. This is possible in the AFI phase by measuring spin wave dispersion relations and comparing those to linear spin-wave theory (LSWT). The acoustic branch of spin waves was previously measured using INS near the magnetic zone center for V_2O_3 and $(V_{0.96}Cr_{0.04})_2O_3$ in the AFI phase [48–50]. The limited range of those data, however, is insufficient to determine the many distinct exchange interactions of the monoclinic phase [50].

Here we report INS measurements of both acoustic and optic branches of spin waves in the AFI phase and incoherent magnetic excitations in the PI phase throughout the Brillouin zone for $(V_{0.96}Cr_{0.04})_2O_3$. At room temperature V_2O_3 has the trigonal (corundum) structure with space group $R\bar{3}c$ (No. 167) while the space group of the low-temperature monoclinic structure is $I 2/a$ (No. 15) with 8 vanadium ions per unit cell. Our new measurements on $(V_{0.96}Cr_{0.04})_2O_3$ allow for the accurate determination of all magnetic exchange interactions in the monoclinic long range ordered AFM state of vanadium sesquioxide. We find moderate ferromagnetic nearest neighbor (nn) and dominant AFM next nearest neighbor (nnn) interactions along the zigzag V chains in the AFI phase (see Fig. 1(c)) in an unfrustrated configuration. Having established the effectiveness of our DFT calculation methods on the AFI phase, we apply them to determine an interacting spin Hamiltonian for the PI phase. A Gaussian approximation applied to this model accounts in detail for our measurements of the short range spin correlations in the PI. This leads to the conclusion that the lack of spin order for temperatures down to 185 K in the PI phase is a consequence of frustrated interactions on the puckered honeycomb lattices that make up the corundum structure.

II. EXPERIMENTAL METHODS

Single crystal samples of $(V_{0.96}Cr_{0.04})_2O_3$ ($T_N = 185$ K) were grown using a skull melter [51]. To increase the sensitivity of our experiment, four single crystals were co-aligned for a total mass of 17 g. In the PI phase at $T = 296$ K, the pseudo-hexagonal lattice constants are $a = b = 4.94$ Å and $c = 14.01$ Å. In the AFI phase at $T = 77$ K, the monoclinic lattice parameters are $a = 7.28$ Å, $b = 4.99$ Å, $c = 5.54$ Å,

($\alpha, \beta, \gamma = [90^\circ, 96.75^\circ, 90^\circ]$) consistent with previous findings [17, 52, 53].

We use both the primitive monoclinic unit cell and the pseudo-hexagonal unit cell to label reciprocal space (Fig. 1). The AFM wave vector $(\frac{1}{2} \frac{1}{2} 0)_H$ in the pseudo-hexagonal unit cell becomes $(0 \ 1 \ 0)_M$ in the monoclinic unit cell. The conversion between pseudo-hexagonal and monoclinic coordinates is given by:

$$\begin{pmatrix} H_M \\ K_M \\ L_M \end{pmatrix} = \begin{pmatrix} \frac{2}{3} & -\frac{2}{3} & -\frac{1}{3} \\ 1 & 1 & 0 \\ \frac{1}{3} & -\frac{1}{3} & \frac{1}{3} \end{pmatrix} \begin{pmatrix} H_H \\ K_H \\ L_H \end{pmatrix}$$

Time-of-flight INS measurements were performed using the SEQUOIA fine-resolution Fermi-chopper spectrometer at the Spallation Neutron Source at ORNL [54, 55]. (Initial measurements were performed at the MARI multidetector chopper spectrometer at the pulsed spallation source at ISIS, UK). With this modern pulsed-neutron spectrometer, we were able to fully map the excitation spectrum of $(V_{0.96}Cr_{0.04})_2O_3$ at three key temperatures indicated in Fig. 1(a). The crystal array was aligned so that the $(-L \ K \ L)_M$ plane was horizontal. The crystal assembly was rotated through 180° in 2° steps about the vertical $(H \ 0 \ H/2)_M$ direction to access a volume of momentum space during the experiment. To balance energy resolution with \mathbf{Q} -space coverage, incident energies of 50 meV and 100 meV were used to collect data at (5 K, 170 K, 205 K) and (5 K, 205 K, 320 K) respectively.

The magnetic neutron scattering cross-section for momentum transfer $\mathbf{Q} = k_i - k_f$ and energy transfer $\hbar\omega$ is given by:

$$\begin{aligned} \frac{d^2\sigma}{d\Omega dE_f} &= N \frac{k_f}{k_i} r_0^2 e^{-2W(\mathbf{Q})} \left| \frac{g}{2} f(\mathbf{Q}) \right|^2 \\ &\times \sum_{\alpha\beta} (\delta_{\alpha\beta} - \hat{Q}_\alpha \hat{Q}_\beta) \mathcal{S}^{\alpha\beta}(\mathbf{Q}, \omega). \end{aligned} \quad (1)$$

where N is the number of hexagonal unit cells, $r_0 = 0.539 \times 10^{-12}$ cm, $f(\mathbf{Q})$ is the magnetic form factor for the V^{3+} ion, and $e^{-2W(\mathbf{Q})}$ is the Debye-Waller factor. Thus, INS directly measures the dynamic spin correlation function (or dynamical structure factor):

$$\begin{aligned} \mathcal{S}^{\alpha\beta}(\mathbf{Q}, \omega) &= \frac{1}{2\pi\hbar} \int dt e^{-i\omega t} \frac{1}{N} \sum_{\mathbf{R}, \mathbf{R}'} e^{i\mathbf{Q}\cdot(\mathbf{R}-\mathbf{R}')} \\ &\times \langle S_{\mathbf{R}}^\alpha(0) S_{\mathbf{R}'}^\beta(t) \rangle. \end{aligned} \quad (2)$$

To enhance statistical quality, we employed the rotational symmetry operations of the PI phase to project the data into an irreducible wedge. In addition, the Mantid software suite [56] was used to subtract an incoherent background (see Appendix A 1). The intensity data was normalized as described in Appendix A 2 so that we report the measured scattering cross section in absolute units as

$$\mathcal{I}(\mathbf{Q}, \omega) = \frac{k_i}{k_f} \frac{1}{N} \frac{d^2\sigma}{d\Omega dE_f} \quad (3)$$

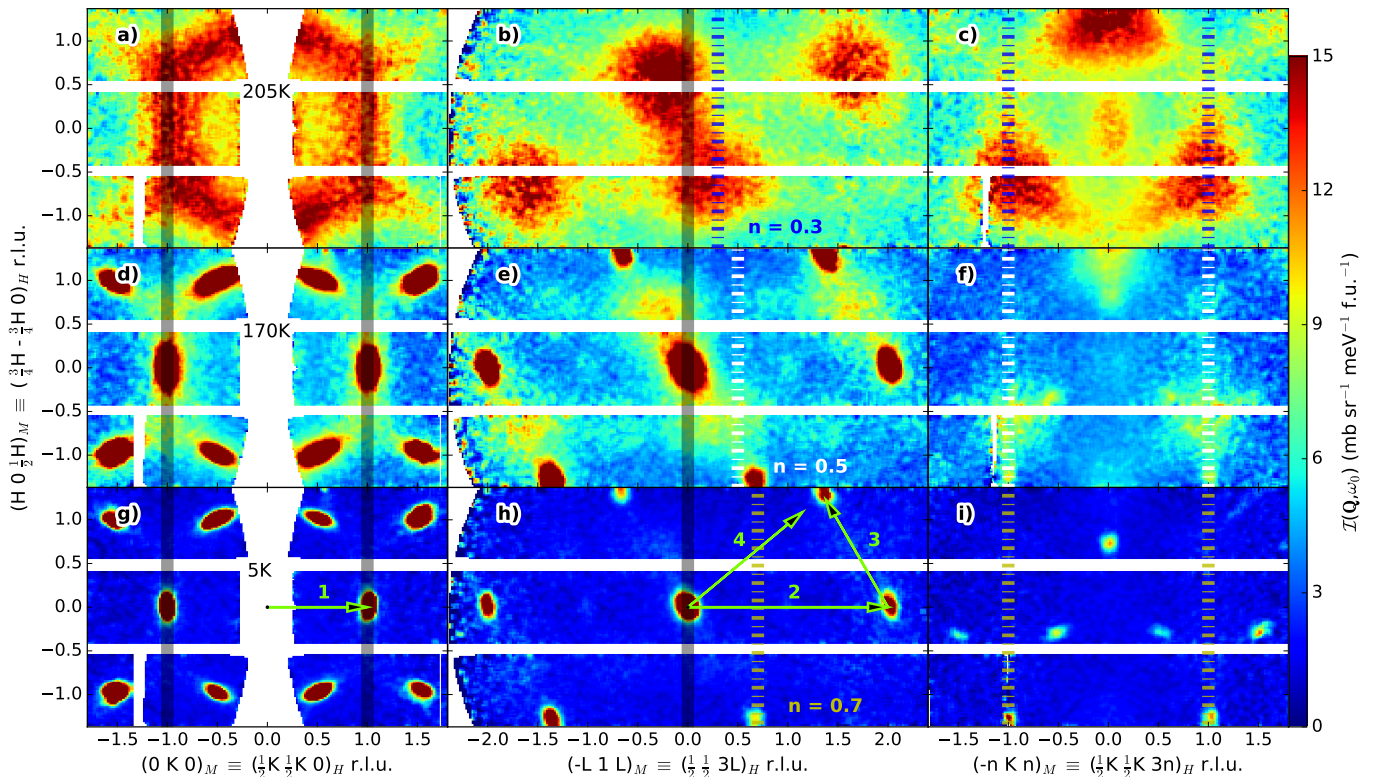


FIG. 2. Constant energy slices of INS data ($E_i = 50$ meV) for $(V_{0.96}Cr_{0.04})_2O_3$; energy transfer averaged from 5 meV $< \hbar\omega_0 < 10$ meV. Each horizontal row shows $\mathcal{I}(\mathbf{Q}, \omega_0)$ for the three temperatures marked along the phase diagram in Fig. 1. The left column (a), (d), and (g) shows $\mathcal{I}(\mathbf{Q}, \omega_0)$ in the pseudo-hexagonal basal plane at the origin ($L = 0$). The center column (b), (e), and (h) covers a plane perpendicular to that of the left column overlapping at the light gray solid lines. The right column shows pseudo-hexagonal planes for $L_H = 3n$ where $n = 0.3, 0.5,$ and 0.7 for frames (c), (f), and (i) respectively as indicated in the center column by the colored dashed lines. Green arrows indicate the 4 high-symmetry directions used in Fig. 3.

III. RESULTS

A. Overview of $\mathcal{S}(\mathbf{Q})$

In Fig. 2 we show the momentum dependence of the spin-correlation function $\mathcal{S}(\mathbf{Q})$ averaged over an energy range of 5-10 meV. The data were acquired with an incident energy of 50 meV at temperatures 205 K, 170 K, and 5 K. The left column (a) (d), and (g) shows $\mathcal{S}(\mathbf{Q})$ for the pseudo-hexagonal basal plane $\mathbf{Q} = (HK0)_H$. It is clear from the low temperature data (g) and (i) that there are three monoclinic domains in the hexagonal basal plane (each 60° apart). Their volume fractions of 56%, 26%, and 18% respectively were determined from Fig. 2(g) and duly incorporated into the forthcoming simulations. The unequal domain population can arise from the symmetry breaking associated with the sample shape and the strain imposed by the sample mounting provisions.

At $T = 205$ K (Fig. 2(a), 2(b), and 2(c)) we observe diffuse scattering that we associate with short range correlated paramagnetic spin fluctuations. Consistent with rhombohedral symmetry, the six-fold structure of magnetic excitations in the pseudo-hexagonal basal plane $L_H = 0$, (Fig 2(a), 2(d), and 2(g)) becomes a three-

fold structure for $L_H \neq 3 \times \text{integer}$ (Fig. 2(c), 2(f), 2(i), and Fig. 4). In these new data we see for the first time the direction, $(H 0 0)_M$ (indicated by the green arrow #3 in Fig. 2(h)), along which coherent spin waves abruptly “melt” into a broad paramagnon excitation at wavevectors located between the acoustic spin wave branches. This may be interpreted as a manifestation of spin-orbital frustration in the PI phase [47].

A dramatic change in the character of the magnetic excitations across the first order AFI to PI phase transition is also apparent in the \mathbf{Q} - E slices of Fig. 3(d). (Note: the qualitative features of Fig. 3(d) persist up to at least 320 K as shown in Appendix B 1, Fig. 7(d)). The sharp excitations near 80 meV energy transfer along the $(-L 1 L)_M$ and $(-2 1 L)_M$ directions that survive to 320 K would appear to be phonons.

B. Exchange Interactions in the AFI Phase

1. Neutron Scattering

Our comprehensive INS data set acquired for $E_i = 100$ meV provides access to both acoustic and optic

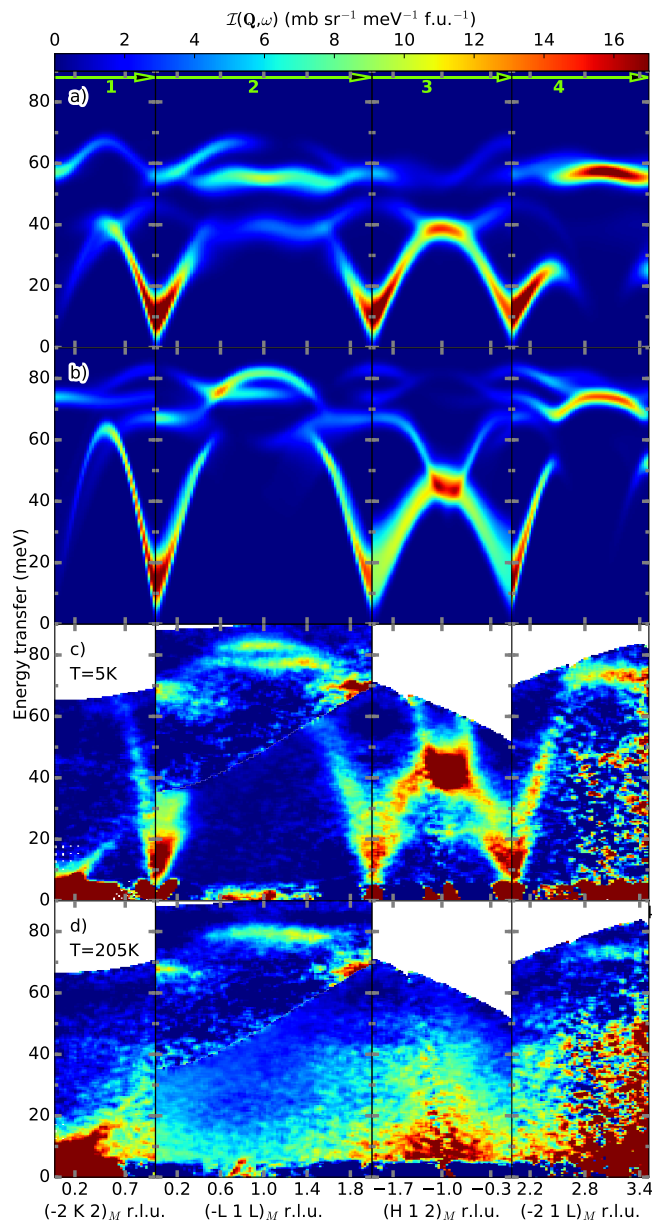


FIG. 3. Neutron scattering intensity associated with spin waves along four high symmetry directions marked in Fig. 2 using (a) DFT calculated exchange constants and (b) exchange constants obtained from fits to the data. (c)(d) INS cross section measured at 5 K and 205 K ($E_i = 100$ meV). Data from multiple Brillouin zones is collected in a reduced Brillouin zone in order to observe the maximum possible range in energy transfer. The data were divided by the squared magnetic form factor for presentation. Also, an incoherent background determined by azimuthal averaging of the same data has been subtracted. (see Appendix A 1).

spin wave excitations from the AFI (Fig. 3(c)). Along all high-symmetry directions, sharp dispersive ridges of magnetic scattering are observed indicative of coherent spin-wave like excitations in the AFI. These can be described as the normal modes of excitation from the or-

distance (\AA)	J_i (meV)	DFT	Neutron	$\text{sgn}(\langle \mathbf{S}_i \cdot \mathbf{S}_j \rangle)$
2.75904	J_α	-1(2)	-6.0(2)	+
2.83083	$J_{\beta 1}$	25(2)	27.7(2)	-
2.91789	$J_{\beta 2}$	9(2)	7.7(2)	-
2.98538	J_γ	3(2)	0.0(2)	+
3.43336	J_ϵ	-9(3)	2.0(2)	-
3.45420	J_δ	4(2)	1.1(2)	-
3.63334	J_η	1(2)	-2.0(2)	+
3.70177	$J_{\zeta 1}$	1(1)	7.1(2)	-
3.76876	$J_{\zeta 2}$	-1(1)	7.1(2)	-
4.22293	J_θ	-4(2)	0	+
4.97765	J_l	3(1)	0	-
5.00240	J_κ	-1(1)	0	+

TABLE I. Magnetic exchange constants for the AFI phase in $(V_{0.96}Cr_{0.04})_2O_3$, obtained from both DFT calculations and direct fitting of the neutron data as described in the main text. Column 5 gives the sign of the indicated correlation $\langle \mathbf{S}_i \cdot \mathbf{S}_j \rangle$ for the AFI structure (see Fig. 1(c)). The consistent negative sign of the product between columns 5 and 6 indicates an unfrustrated magnet.

dered state of an antiferromagnet described by a spin Hamiltonian of the form:

$$\mathcal{H}_{mag} = \sum_{i,j} J_{ij} \mathbf{S}_i \cdot \mathbf{S}_j + \sum_i D(S_i^z)^2. \quad (4)$$

Here J_{ij} are exchange constants for interaction between spins i and j that we approximate as Heisenberg like (isotropic in spin-space). The symmetry inequivalent exchange interactions in the PI and AFI phases are defined in Fig. 1(b)(c). A derivation of the corresponding spin wave dispersion relation in the monoclinic AFI phase was first presented in Ref. [50]. For simplicity, the measured 4.8 meV energy gap in the spin-wave excitation spectrum is wholly attributed to a uni-axial single ion anisotropy term $D = 0.13$ meV, even though exchange anisotropy must also be present [48, 50].

For a given set of exchange constants, the inelastic neutron scattering cross section associated with spin wave excitations from the AFI state was calculated with linear spin wave theory (LSWT) using the SpinW program [57] and then convoluted with the energy dependent instrumental resolution function [54, 55]. By comparing the measured and calculated spectra along the four high symmetry directions (Fig. 2(g) and 2(h)), we inferred the best fit exchange parameters listed in Table I. The INS that we associate with spin-waves (Fig. 3(c)) is well accounted for by the model (Fig. 3(b)), which gives confidence that the corresponding exchange Hamiltonian describes magnetic interactions within the AFI phase.

2. Density Functional Theory

DFT electronic structure calculations for the monoclinic AFI were performed using the $T = 15$ K structure of Rozier *et al.* [58] with the full potential local orbital

(FPLO) basis set [59] and the GGA functional [60]. We obtained up to 9th near neighbor exchange constants by mapping total energy differences of various magnetic configurations to the Heisenberg model [61]. Exchange constants up to V-V distances of 3.76 Å shown in Table I are connected by superexchange paths involving one oxygen. From a perturbation perspective, these are all of the same order so that any of them could be important. For exchange constants with distances beyond 4.22 Å (J_θ etc.), the superexchange paths become more complex and the magnitude of the exchange constants can be expected to be significantly smaller.

Exchange constants were calculated with high precision for pure V_2O_3 . The AFI phase measurements of exchange constants conveniently serve to benchmark these *ab initio* calculations of exchange interactions. We found that to achieve quantitative agreement with the experimental J values, in particular the sign of J_α (see Appendix B 1), accounting for the 4% Cr ($S = 3/2$) doping in the sample was necessary. Introducing Cr-doping into the DFT calculations is quite challenging and leads to significantly higher statistical error ranges. Two complementary approaches were employed: (1) Replacing one out of every 25 V^{3+} ions with a Cr^{3+} ion and (2) increasing the average nuclear charge from $Z = 23$ (pure V_2O_3) to $Z = 23.04$ ($(V_{0.96}Cr_{0.04})_2O_3$) and using the virtual crystal approximation. Both of these approaches can deliver reasonable indications concerning the effect of Cr doping. We found that in both cases the Cr-doping indeed introduces a tendency towards FM $J_\alpha < 0$, which agrees much better with the experimental data.

The DFT calculated exchange constants for $(V_{0.96}Cr_{0.04})_2O_3$ in the AFI phase with $U = 3$ eV are listed in the 3rd column of Table I. The simulated $\mathcal{S}(\mathbf{Q}, \omega)$ from these *ab initio* exchange parameters using LSWT as implemented in SpinW is shown in Fig. 3(a). Considering this is a first principles result, the similarity with measured INS in Fig. 3(c) is remarkable. Limitations of DFT and LSWT for this low spin ($S = 1$) quantum magnet may contribute to discrepancies between the experimental data and theory. The comparison between experiment and *ab initio* theory is also favorable in terms of the inferred exchange constants (compare 3rd and 4th columns of Table I). While next-nearest neighbor exchange interactions linking neighboring pseudo-honeycomb lattice planes seem to be problematic, the measured in-plane interactions are consistently accounted for by DFT.

C. Exchange Interactions in the PI Phase

Having shown that DFT can determine the exchange interactions in the AFI phase of $(V_{0.96}Cr_{0.04})_2O_3$, we use this same method to determine the exchange interactions in the PI phase, where the absence of spin wave excitations makes it harder to infer the exchange interactions from neutron scattering measurements.

distance (Å)	J_j	$\equiv J_i$	DFT (meV)
2.71072	J_1	J_α	-0.3(6)
2.87799	J_2	$J_{\beta 1}, J_{\beta 2}, J_\gamma$	8.5(3)
3.46255	J_3	J_ϵ, J_δ	0.6(3)
3.68774	J_4	$J_\eta, J_{\zeta 1}, J_{\zeta 2}$	0.0(2)
4.29734	J_5	J_θ	-1.2(7)
4.94240	J_6	J_ι, J_κ	1.7(2)

TABLE II. DFT Calculated exchange constants for the PI phase in $(V_{0.96}Cr_{0.04})_2O_3$. Column 3 shows the corresponding exchange constants for the AFI phase.

DFT calculations were performed for the high temperature structure of Rozier *et al.* [58] including Cr doping because, as mentioned earlier, we found this to be important particularly for the nearest neighbor J_α interaction in the AFI. The calculation results for the first six exchange constants (identified by their bond distances) are shown in Table II. The corresponding exchange paths (bond vectors) are shown in Fig. 1(b). These exchange constants yield a Curie-Weiss temperature Θ_{CW} of -400 K, which is consistent with the experimental value of -350 K [62].

The fact that the magnetic correlation length is on the atomic scale (Fig. 4) even for $T < \frac{1}{2}|\Theta_{CW}|$ indicates the PI phase is magnetically frustrated. Let us now examine whether or not the PI phase interactions inferred from DFT can account for the specific short ranged nature of the spin correlations. The self-consistent Gaussian approximation (SCGA) was previously shown to be effective for determining the equal time spin-correlation function, $\mathcal{S}(\mathbf{Q})$, of geometrically frustrated magnets [63]. Based on a spherical spin model [64], the softened spin configurations are weighted by the Boltzmann factor $e^{-\beta\mathcal{H}}$:

$$\beta\mathcal{H} = \frac{1}{2} \sum_{ij} (\beta \sum_n J_n A_{ij}^{(n)} + \lambda \delta_{ij}) s_i s_j, \quad (5)$$

where s_i denotes one component of the spin vector \mathbf{S}_i and $A^{(n)}$ contains the interaction between n^{th} -nearest neighbors. The Lagrangian multiplier λ is determined self-consistently to ensure the average spin length $\langle s_i^2 \rangle = 1/3$. The rhombohedral structure of the PI is broken into six hexagonal sublattices and the Fourier transform is taken to obtain quadratic interaction between sublattices. In reciprocal space, the condition on λ is expressed as the trace of the inverse interaction matrix. The spin correlator as the two-body propagator is calculated at certain momentum transfers \mathbf{Q} . We applied the SCGA method to determine spin correlations at $T = 205$ K, where fluctuations of the classical spins are thermal. The calculated equal time spin correlation function is in remarkable agreement with the experimental INS data (see the matching broad features shown in Fig. 4).

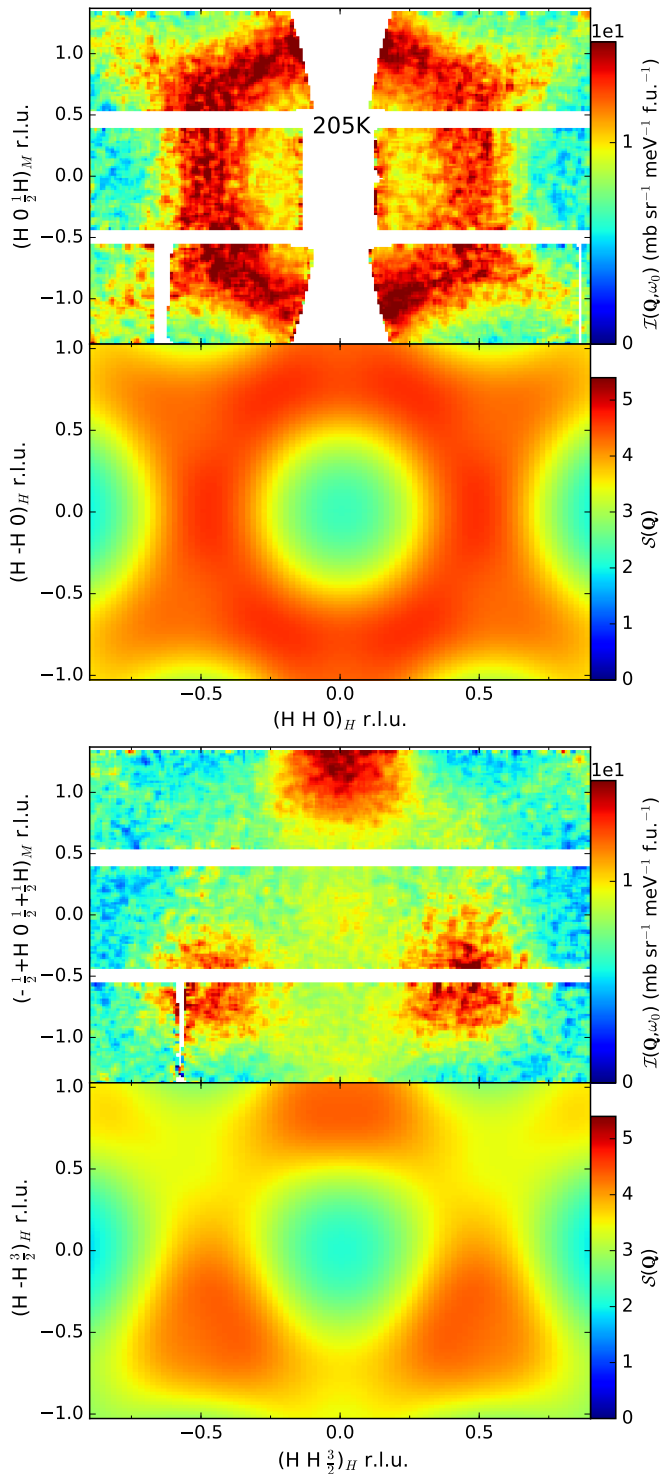


FIG. 4. Neutron scattering intensity from $(\text{V}_{0.96}\text{Cr}_{0.04})_2\text{O}_3$ at 205 K at $\hbar\omega_0 = 7.5$ meV (averaging range = [5,10] meV) for wavevector transfer within pseudo-hexagonal basal planes (as in Fig. 2) at offsets along the pseudo-hexagonal c -axis of $L_H = 0$ and $L_H = 1.5$. These experimental data are compared with the calculated dynamic spin correlation function $S(\mathbf{Q})$ for the DFT calculated exchange constants of the PI phase given in Table II.

IV. ANALYSIS AND DISCUSSION

A. Frustrated Interactions in the PI Phase

With the detailed set of exchange constants at hand (Table II) we are in a position to examine the nature of the frustrated PI phase. The two strongest exchange constants, J_2 and J_6 (see Fig. 1(b)), form quasi-honeycomb lattices with competing nearest neighbor (J_2) and next nearest neighbor (J_6) interactions. While J_2 favors bipartite AFM order where each spin is anti-parallel to its nearest neighbors, J_6 stabilizes a stripy phase [65]. For $(\text{V}_{0.96}\text{Cr}_{0.04})_2\text{O}_3$ the DFT calculations yield $J_6/J_2 \sim 0.20$ which place the PI phase in the valence bond crystal or spin liquid phase of the frustrated honeycomb model [65, 66]. The correlation length for such a model may be sufficiently short that the only significant inter-layer interactions (which are J_5 , J_3 , and J_1 in order of their strength) are rendered ineffective. The importance of the next nearest interaction J_6 within the honeycomb layers of pure V_2O_3 was previously noted based on GGA+U calculations [23].

Examining the \mathbf{Q} - E slices for the PI phase in Fig. 3(d) reveals factorization of the \mathbf{Q} and E dependence of the dynamic spin correlation function with a 40 meV bandwidth in energy that resembles the Weiss temperature and greatly exceeds $k_B T$. Such dynamic correlations resemble a number of strongly frustrated magnets that are described as quantum paramagnets such as ZnCr_2O_4 [6] and $\text{SrCr}_9\text{pGa}_{12-9\text{p}}\text{O}_{19}$ [67].

The SCGA method breaks down at low temperatures when the interacting spin model develops magnetic order. A finite size scaling calculation estimates that ordering temperature to be ~ 10 K. Comparison to the Curie-Weiss temperature of ~ 400 K yields a frustration index of $f = 40$, indicating a high degree of magnetic frustration in the PI phase. The $T \approx 10$ K phase transition anticipated for the PI spin Hamiltonian is however preempted in $(\text{V}_{0.96}\text{Cr}_{0.04})_2\text{O}_3$ at $T_N = 185$ K by the first order magneto-structural transition that relieves magnetic frustration and gains magnetic exchange energy at the expense of lattice strain energy. DFT and neutron scattering indicates the magnetic exchange interactions are significantly modified at this transition (compare Tables I and II). In particular, the three identical nearest neighbor interactions within the PI honeycomb lattices (DFT: $J_2 = 8.5(3)$ meV) split into three distinct interactions in the AFI phase (DFT[Neutron]: $J_{\beta_1} = 25(2)[27.7(2)]$ meV, $J_{\beta_2} = 9(2)[7.7(2)]$ meV, and $J_\gamma = 3(2)[0.0(2)]$ meV). This relieves frustration and gives way to the stripy ordered phase favored by the next nearest neighbor interaction (DFT: $J_6 = 1.7(2)$ meV).

B. Unfrustrated Interactions in the AFI Phase

Referring to the experimental exchange constants in the 4th column of Table I, we note they are consistently

un-frustrated: Spins that interact antiferromagnetically (ferromagnetically) are also antiferromagnetically (ferromagnetically) correlated in the ordered state (see column 5 of Table I). Thus, while exchange interactions in the PI phase realize a frustrated honeycomb antiferromagnet as determined by comparing nearest and next nearest neighbor interactions, the modified nearest neighbor interactions in the AFI phase are all simultaneously satisfied in the long range ordered magnetic state (i.e., the signs of the 4th and 5th columns of Table I are consistently opposite).

The raw experimental evidence for un-frustrated interactions is the large bandwidth of magnetic excitations in the AFI phase (80 meV). Because the bandwidth exceeds $k_B T_N$ by a factor of four, the collapse of the ordered state upon heating occurs before significant thermal population of spin waves. Also, there is no build up of magnetic correlations upon cooling the frustrated PI towards the $T_N = 185$ K phase transition. Nonetheless comparison of Fig. 3(c) and Fig. 3(d) shows a clear upward shift of magnetic spectral weight, which indicates lowering of the magnetic exchange energy as frustration is relieved at the first order PI to AFI transition.

The nearest neighbor inter-plane interaction between face-sharing vanadium atoms, $J_\alpha = -6.0(2)$ meV, is the main FM interaction that favors FM sheets in the AFI. Our results confirm that J_β and J_ζ are stronger than J_α , and therefore suggest that superexchange via V-O-V paths contribute to the realization of a strong ferromagnetic alignment for the vertical V pairs. The values of $J_\alpha = -4.1$ meV and $J_{\beta 1} = 18.4$ meV determined by the LDA+ U study of [38] are consistent with these values and the author's suggestion that the next near neighbor exchange interactions are significant is consistent with the large $J_\zeta = 7.1(2)$ meV that we obtain.

It is interesting to compare experimental and *ab initio* exchange interactions for $(V_{0.96}Cr_{0.04})_2O_3$ with those of pure Cr_2O_3 determined by Samuelsen *et al.* [68]. They showed that only the first two exchange interactions are significant in Cr_2O_3 , with the nearest neighbor interaction being dominant at 7.5 meV. Thus the range of interactions in $(V_{0.96}Cr_{0.04})_2O_3$ is considerably longer than in Cr_2O_3 , which is broadly consistent with greater $3d$ -electron delocalization in proximity to the Mott transition of V_2O_3 .

V. CONCLUSION

In summary, magnetic exchange interactions in the AFI phase of $(V_{0.96}Cr_{0.04})_2O_3$ were determined with INS measurements of both acoustic and optic spin waves throughout the monoclinic Brillouin zone. Ordered by magnitude the leading interactions are J_β and J_ζ , which are both antiferromagnetic, and the nearest neighbor interlayer interaction J_α , which is ferromagnetic (Fig. 1(c)). These and indeed all interactions in the AFI phase are satisfied within the observed low T magnetic

structure. In the PI phase diffuse inelastic magnetic neutron scattering and DFT combined with a Gaussian approximation to the spin correlation function show this is a cooperative paramagnet with frustrated near (J_2) and next nearest neighbor (J_6) interactions within the puckered honeycomb layers that form the corundum structure (Fig. 1(b)). We infer that the strong suppression of magnetic order that results from this frustration is key to preventing the AFI phase from engulfing the Mott-like PM to PI phase boundary in V_2O_3 .

The insulating states of compounds with an experimentally accessible Mott-like phase boundary including $Ni(S_{1-x}Se_x)_2$, [69] $GaTa_4Se_8$ [70, 71], and the quasi-two-dimensional organic systems $\kappa - (ET)_2Cu[N(CN)_2]Cl$, $\kappa - (ET)_2Cu_2(CN)_3$, and $EtMe_3Sb[Pd(dmit)_2]_2$ [13] have all been found to be magnetically frustrated. Conversely the spin-liquid-like properties of the latter two compounds have been associated with the increased range and nature of spin-spin interactions near the Mott transition. The present work on $(V_{1-x}Cr_x)_2O_3$ reinforces these interesting links between frustrated magnetism and the Mott transition.

VI. ACKNOWLEDGEMENTS

The authors would like to acknowledge helpful discussions with Sandor Toth, Arnab Banerjee, and Oleg Tchernyshyov. R.V. thanks Frank Lechermann for useful discussions. This project was supported by UT-Battelle LDRD #3211-2440. Work at IQM was supported by the U.S. Department of Energy, Office of Basic Energy Sciences, Division of Materials Sciences and Engineering through Grant No. DE-FG02-08ER46544. This research used resources at the Spallation Neutron Source, a DOE Office of Science User Facility operated by the Oak Ridge National Laboratory (ORNL). This research used resources of the National Energy Research Scientific Computing Center, a DOE Office of Science User Facility supported by the Office of Science of the U.S. Department of Energy under Contract No. DE-AC02-05CH11231. The work at RUC was supported by the National Basic Research Program of China Grants No. 2012CB921700, No. 2011CBA00112, and by the National Science Foundation of China Grants No. 11034012, No. 11190024. The work in Frankfurt was supported by the Deutsche Forschungsgemeinschaft under Grant SFB/TRR 49.

Appendix A: Data Processing Methods

1. Incoherent background subtraction

With the new capabilities of the Mantid Data Analysis Software [56], it is possible to subtract a ϕ independent (ϕ being the azimuthal rotation angle of \mathbf{k}_f around \mathbf{k}_i) background signal from the 4D $\mathcal{S}(\mathbf{Q}, \omega)$ data. This is done by taking a judiciously sampled powder average

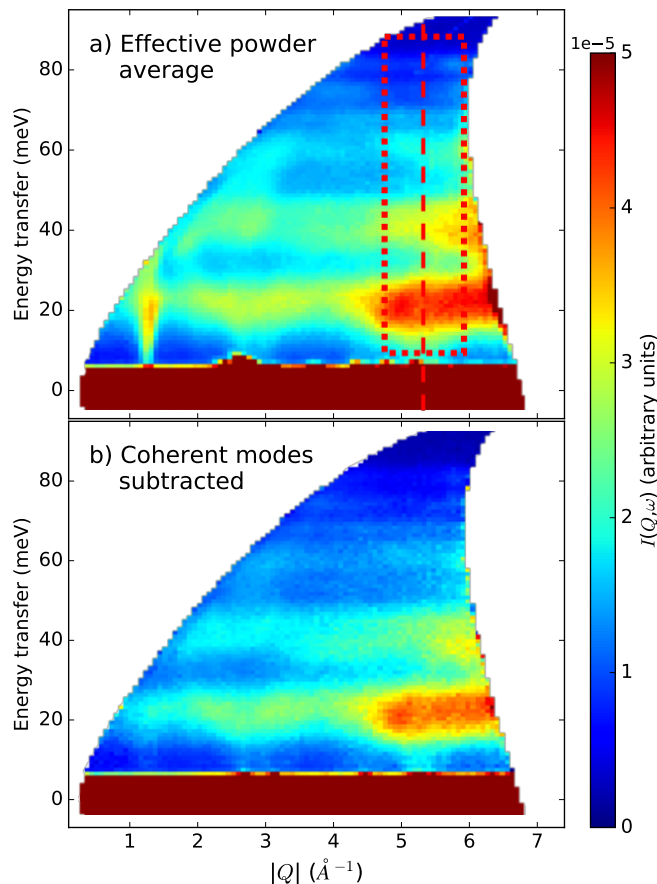


FIG. 5. (a) An effective powder average (taken over all collected sample rotation angles) for the single crystal $(V_{0.96}Cr_{0.04})_2O_3$ $T = 5$ K data used in the main text. The dashed red lines represent a 1D cut of the phonon DOS used in Fig. 6. (b) Powder average of the same data excluding scattering that depends on the azimuthal angle, ϕ . Such filtered data were utilized as background.

of the $S(\mathbf{Q},\omega)$ including only incoherent ϕ -independent components and excluding coherent ϕ -dependent components. (See Fig. 5). Once this special powder average is obtained it can readily be subtracted from the $S(\mathbf{Q},\omega)$ data as a background.

2. Phonon density of states (DOS) calculations

Normalization of the scattering data was achieved through the incoherent phonon scattering cross section. The neutron weighted phonon DOS $g^{(n)}(\omega)$ was theoretically calculated with VASP + Phonopy for the AFI phase of V_2O_3 . This is shown as a solid green line in Fig. 6 in units of $\text{meV}^{-1}\text{f.u.}^{-1}$ (5 atoms per formula unit).

The experimental phonon DOS was obtained by first taking a constant- Q cut through the effective powder average (generated by averaging over all collected sample rotation angles) of the $T = 5$ K INS spectra. In this case the cut is taken by integrating in a rectangular area at

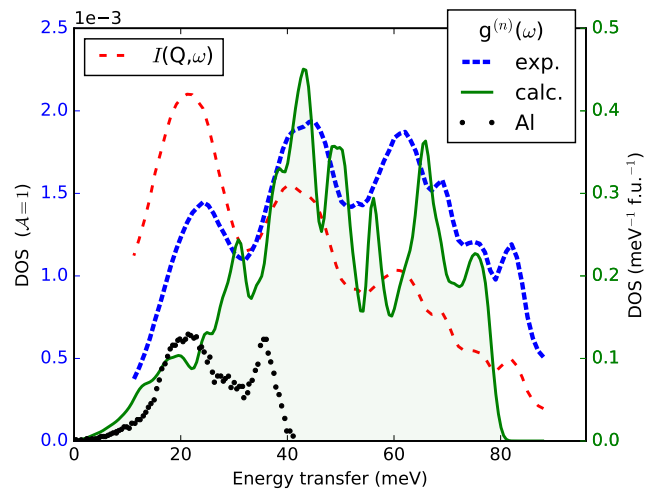


FIG. 6. Phonon DOS for $(V_{0.96}Cr_{0.04})_2O_3$ extracted from an effective powder average of the INS data (See Fig. 5(a) and description below). This is compared with theoretical phonon DOS calculated for V_2O_3 in the low-temperature AFI phase. Also shown is the phonon DOS for aluminum from Ref. [72].

high momentum transfer centered around $|Q| = 5.3 \text{ \AA}^{-1}$, as shown by the dashed red lines in Fig. 5(a). The result of this integration is plotted as the dashed red line (not to scale) in Fig. 6. This cut from the experimental data can then be converted into the neutron weighted generalized phonon DOS $g^{(n)}(\omega)$ (the blue line in Fig. 6) via the following formula:

$$g^{(n)}(\omega) = \frac{\mathcal{A}I(Q, \omega)}{\frac{\sigma_{V_2O_3}}{4\pi} \left(\frac{(\hbar Q)^2}{2M} / \hbar\omega \right) (n(\omega, T) + 1)} \quad (\text{A1})$$

where $I(Q, \omega)$ is the proton charge normalized detector counts binned in $Q = |\mathbf{Q}|$ and ω , $n(\omega, T) = [e^{\beta\hbar\omega} - 1]^{-1}$, $\sigma_{V_2O_3} = 22.88$ barn/f.u. is the total scattering cross section (coherent plus incoherent) per formula unit for the sample, and M is the mass per formula unit. \mathcal{A} is the normalization constant, which was adjusted to achieve the best overlap between the experimental and theoretical $g^{(n)}(\omega)$ traces in Fig. 6. This procedure yields $\mathcal{A} = 200(50)$ barn \times coulomb/meV/counts. Using this normalization factor the conversion of raw scattering intensities to a normalized cross section is as follows: $\mathcal{I}(\mathbf{Q}, \omega) = \mathcal{A}I(\mathbf{Q}, \omega)$.

Some of the discrepancy between the experimental and theoretical $g^{(n)}(\omega)$ may arise from contributions to scattering intensity from the aluminum can sample holder. Previously measured phonon DOS for aluminum [72] shows its strongest peak is near 20 meV energy transfer. This is consistent with the extra intensity seen near 20 meV in the experimental $g^{(n)}(\omega)$ when comparing with the theoretical $g^{(n)}(\omega)$ for V_2O_3 . We estimate this normalization procedure is accurate to within 25%.

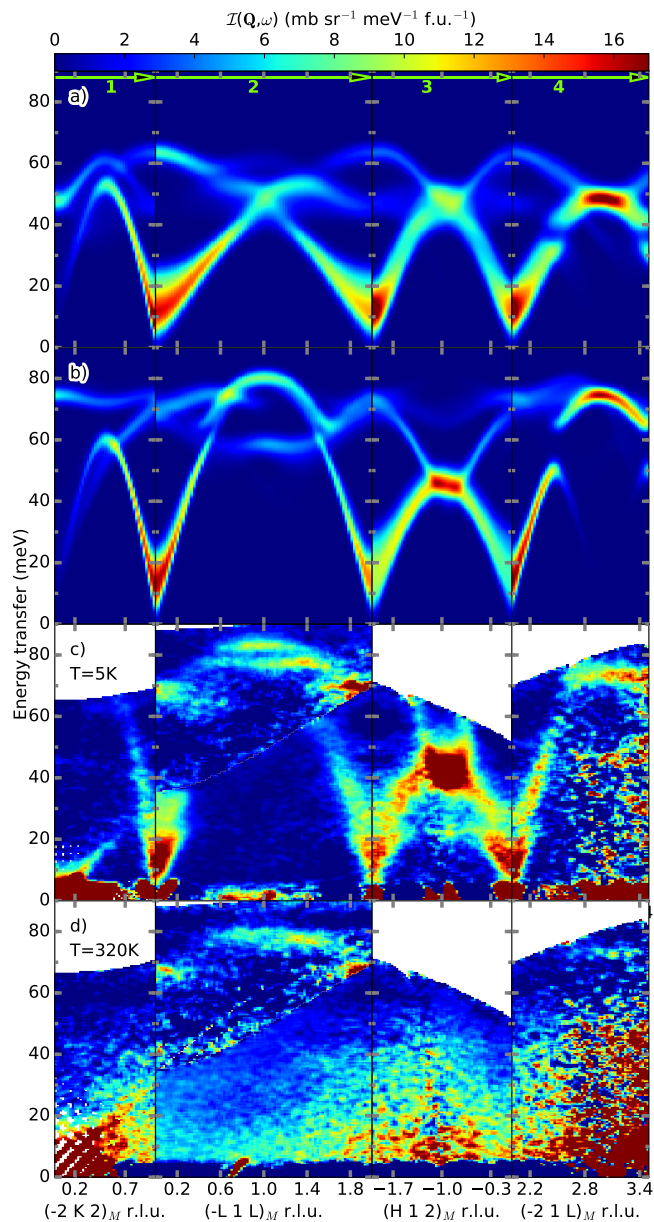


FIG. 7. (a)(b) Neutron scattering intensity associated with spin waves along four high symmetry directions marked in Fig. 2 calculated with SpinW [57] for exchange constants shown in Table III. (c)(d) INS cross section measured at 5 K and 320 K ($E_i = 100$ meV). Data from multiple Brillouin zones is collected in a reduced Brillouin zone in order to observe the maximum possible range in energy transfer. The data were divided by the squared magnetic form factor for presentation. Also, an incoherent background was subtracted from the data as described earlier.

Appendix B: Extended Data Modeling

1. DFT calculated exchange constants

The initial DFT calculations of exchange interactions were performed for pure monoclinic V_2O_3 . These yielded

J_i	distance (\AA)	Pure V_2O_3	Fig. 7(b)
J_α	2.75904	2.8(3)	-2.7
$J_{\beta 1}$	2.83083	28.7(3)	27.5
$J_{\beta 2}$	2.91789	12.4(3)	7.7
J_γ	2.98538	-2.3(3)	2.8
J_ϵ	3.43336	-3.9(5)	-6.1
J_δ	3.45420	3.5(3)	1.9
J_η	3.63334	0.6(3)	-1.0
$J_{\zeta 1}$	3.70177	2.5(2)	2.5
$J_{\zeta 2}$	3.76876	-0.3(2)	6.5
J_θ	4.22293	0.8(3)	-1.6
J_l	4.97765	0.4(2)	2.0
J_κ	5.00240	1.7(2)	0.0

TABLE III. Exchange constants for monoclinic pure V_2O_3 (in meV) calculated with DFT using two unit cells as explained in the text below. The resultant INS cross sections from the spin waves with these exchange constants are shown in Fig. 7(a). Also, shown in Fig. 7(b) is the LSWT result using the set of DFT calculated exchange parameters from Table I for $(V_{0.96}Cr_{0.04})_2O_3$ with adjustments made (as described in the text) within statistical error tolerances, except for the value of $J_{\zeta 2}$ shown in bold.

results with smaller statistical errors than when including the effects of chromium doping. As mentioned in the main text, these calculations were performed with the full potential local orbital (FPLO) basis set [59] and the GGA functional [60]. Total energies for large sets of different spin configurations were calculated with GGA+ U using the atomic limit double counting correction [73]. We fix $J_H = 0.68$ eV [74] and vary U . For the LSWT modeling, we only employ the $U = 3$ eV values.

The calculation was carried out to obtain the first 12 exchange constants of monoclinic pure V_2O_3 by combining the total energies of two supercells: (1) A $2 \times 2 \times 2$ supercell with $P\bar{1}$ symmetry, which leaves 8 V^{3+} ions inequivalent (2) A $1 \times \sqrt{2} \times \sqrt{2}$ with $P\bar{1}$ symmetry, also containing 8 inequivalent V^{3+} ions. While neither of the two structures allow for resolution of all 12 exchange constants, the combined equations have enough information.

The exchange constants resulting from this calculation at $U = 3$ eV are listed in the 3rd column of Table III. The equations determined for the spin configurations analyzed indicate some correlations between the inferred exchange constants, in particular between J_α and J_ϵ . Statistical errors are on the order of 0.5 meV, providing a reasonable degree of confidence for all except the smallest exchange constants, $J_{\zeta 2}$ and J_l . The resultant neutron scattering intensity obtained from these exchange constants through LSWT as implemented in SpinW [57] are plotted in Fig. 7(a). We note that, as expected from the aforementioned correlations, it is possible to exchange J_α and J_ϵ with little effect on the overall dispersion, especially for the ideal case of a single domain sample. As for $(V_{1-x}Cr_x)_2O_3$, almost all of these calculated exchange constants are satisfied in the AFI phase.

We now return to the DFT calculated exchange con-

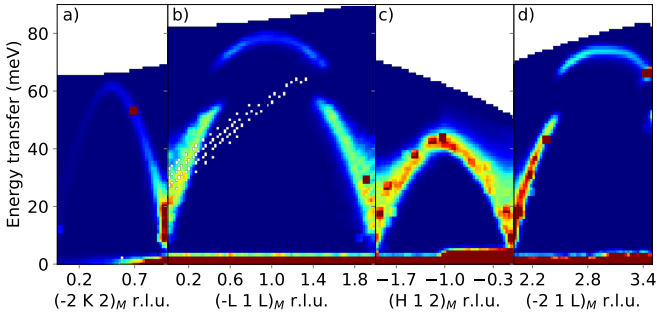


FIG. 8. MCViNE simulation of the same $\mathcal{I}(\mathbf{Q}, \omega)$ slices shown in Fig. 3(c) and Fig. 7(c). This simulation takes into account all instrumental effects and shows similar linewidth broadening as in the experimental scattering data.

stants for $(\text{V}_{0.96}\text{Cr}_{0.04})_2\text{O}_3$ listed in Table I. As the statistical error in these is around 2 meV, liberty may be taken to make adjustments within these error ranges and bring them closer to the experimentally fitted values. Such optimally adjusted J values are shown in column 4 of Table III. The resultant neutron intensity is plotted in Fig. 7(b). The only adjustment that must stray beyond the tolerances of the statistical errors from Table I in order to achieve consistency with experiment is the value of $J_{\zeta 2}$ (set as 6.5 meV, shown in bold). The DFT methods may have trouble accounting for this particular interaction due to accuracy limitations of the structural model for such long-range superexchange interactions. Nevertheless, we have a new set of exchange parameters which yields spin wave dispersions consistent with the scattering data. Comparison of column 4 in Table I and Table III indicate the experimental error bar in the determination of these exchange constants from neutron scattering data. We note that in the original fitting, we set $J_{\theta} = J_l = J_{\kappa} = 0$ to reduce the number of fitting parameters. Thus, when working combinations of 12 exchange constants for ab initio DFT calculations instead of 9 for our standard direct fitting, we may expect increased correlated uncertainties in the extracted exchange constants. Nonetheless, the overall qualitative trends and magnitudes of the two presented sets of exchange constants which fit the data are similar, thus preserving the validity of the associated discussion in the main text.

2. MCViNE simulation for determining instrumental effects on data

Looking at Fig. 3(a)-3(c) as well as Fig. 7(a)-7(c), more broadening is noticeable in the experimental data (c) of the acoustic magnon branches than is predicted by the simulations (a)(b) with LSWT via SpinW, despite using consistent averaging ranges to produce each slice. To determine whether this reflects the physics of V_2O_3 or an instrumental effect, we performed Monte Carlo ray-tracing simulations of the experiment using MCViNE [75]. The

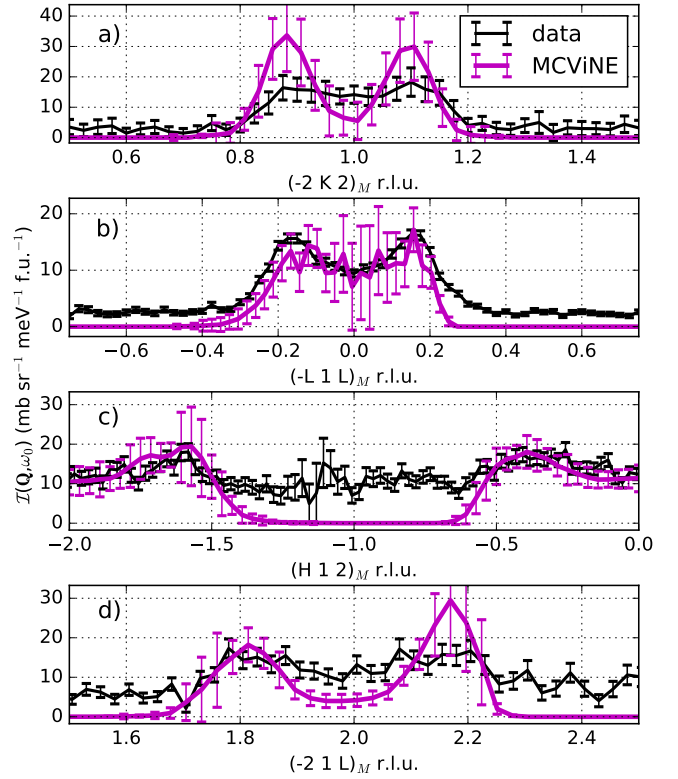


FIG. 9. Constant energy cuts at $\hbar\omega_0 = 30$ meV (averaging range = $[29, 31]$ meV) through the experimental data from Fig. 3(c) and the MCViNE simulation from Fig. 8. The width of the peaks are the same within error.

simulation follows the routine MCViNE simulation procedure [75] that involves four steps. First the neutron beam ~ 12 cm upstream of the sample position was simulated. In the second step, the simulated beam was scattered by a virtual sample, which is a plate of 4.6 cm x 4.6 cm x .57 cm and has a scattering kernel of a dispersion surface (see the supplemental materials of Ref. [75]) specified by an analytical dispersion function. The virtual sample is aligned as in the experiment and the goniometer angle was swept from -90° to 90° in 2° steps. In the third step, the interception of simulated scattered neutrons by the SEQUOIA [54] detector system were simulated and a series of NeXus files were generated. In the last step, the NeXus files were reduced and slices were taken as for the real neutron scattering data. The results are shown in Fig. 8. By examining constant energy cuts as shown in Fig. 9, one sees that the broadening of the acoustic spin waves in the actual neutron data is for the most part reproduced by this simulation of realistic instrumental effects. There is however, a tendency towards sharper peaks in the simulation (especially in Fig. 9(a) and 9(d)). This indicates some spin-wave damping, which is not unexpected for a quantum magnet near the metal insulator transition. But overall, the coherent magnon approximation provides a reasonable description of the full data set.

- [1] I. Leonov, V. I. Anisimov, and D. Vollhardt, *Phys. Rev. B* **91**, 195115 (2015).
- [2] A. I. Frenkel, D. M. Pease, J. I. Budnick, P. Metcalf, E. A. Stern, P. Shanthakumar, and T. Huang, *Phys. Rev. Lett.* **97**, 195502 (2006).
- [3] B. A. Frandsen, L. Liu, S. C. Cheung, Z. Guguchia, R. Khasanov, E. Morenzoni, T. J. Munsie, A. M. Hallas, M. N. Wilson, Y. Cai, *et al.*, *Nature communications* **7** (2016), 10.1038/ncomms12519.
- [4] F. Lechermann, N. Bernstein, I. I. Mazin, and R. Valentí, *arXiv preprint arXiv:1801.08906* (2018).
- [5] O. Tchernyshyov, R. Moessner, and S. L. Sondhi, *Phys. Rev. Lett.* **88**, 067203 (2002).
- [6] S.-H. Lee, C. Broholm, T. H. Kim, W. Ratcliff, and S.-W. Cheong, *Phys. Rev. Lett.* **84**, 3718 (2000).
- [7] S.-H. Lee, D. Louca, H. Ueda, S. Park, T. J. Sato, M. Isobe, Y. Ueda, S. Rosenkranz, P. Zschack, J. Íñiguez, Y. Qiu, and R. Osborn, *Phys. Rev. Lett.* **93**, 156407 (2004).
- [8] S.-H. Lee, H. Takagi, D. Louca, M. Matsuda, S. Ji, H. Ueda, Y. Ueda, T. Katsufuji, J.-H. Chung, S. Park, S.-W. Cheong, and C. Broholm, *Journal of the Physical Society of Japan* **79**, 011004 (2010).
- [9] D. B. McWhan, A. Menth, J. P. Remeika, W. F. Brinkman, and T. M. Rice, *Phys. Rev. B* **7**, 1920 (1973).
- [10] R. M. Moon, *Phys. Rev. Lett.* **25**, 527 (1970).
- [11] Z. A. Kelly, M. J. Gallagher, and T. M. McQueen, *Phys. Rev. X* **6**, 041007 (2016).
- [12] I. I. Mazin, H. O. Jeschke, F. Lechermann, H. Lee, M. Fink, R. Thomale, and R. Valentí, *Nature communications* **5**, 4261 (2014).
- [13] T. Furukawa, K. Miyagawa, H. Taniguchi, R. Kato, and K. Kanoda, *Nature Physics* **11**, 221 (2015).
- [14] Y. Feng, R. Jaramillo, A. Banerjee, J. M. Honig, and T. F. Rosenbaum, *Phys. Rev. B* **83**, 035106 (2011).
- [15] Y. Zhou, K. Kanoda, and T.-K. Ng, *Rev. Mod. Phys.* **89**, 025003 (2017).
- [16] D. B. McWhan, T. M. Rice, and J. P. Remeika, *Phys. Rev. Lett.* **23**, 1384 (1969).
- [17] D. B. McWhan and J. P. Remeika, *Phys. Rev. B* **2**, 3734 (1970).
- [18] Y. Ueda, K. Kosuge, and S. Kachi, *Journal of Solid State Chemistry* **31**, 171 (1980).
- [19] H. Kuwamoto, J. M. Honig, and J. Appel, *Phys. Rev. B* **22**, 2626 (1980).
- [20] S. A. Carter, T. F. Rosenbaum, J. M. Honig, and J. Spalek, *Phys. Rev. Lett.* **67**, 3440 (1991).
- [21] M. Yethiraj, *Journal of Solid State Chemistry* **88**, 53 (1990).
- [22] P. Limelette, A. Georges, D. Jérôme, P. Wzietek, P. Metcalf, and J. Honig, *Science* **302**, 89 (2003).
- [23] D. Grieger and M. Fabrizio, *Phys. Rev. B* **92**, 075121 (2015).
- [24] C. Castellani, C. R. Natoli, and J. Ranninger, *Phys. Rev. B* **18**, 4945 (1978); *Phys. Rev. B* **18**, 4967 (1978); *Phys. Rev. B* **18**, 5001 (1978).
- [25] M. J. Rozenberg, G. Kotliar, H. Kajueter, G. A. Thomas, D. H. Rapkine, J. M. Honig, and P. Metcalf, *Phys. Rev. Lett.* **75**, 105 (1995).
- [26] W. Bao, C. Broholm, S. A. Carter, T. F. Rosenbaum, G. Aeppli, S. F. Trevino, P. Metcalf, J. M. Honig, and J. Spalek, *Phys. Rev. Lett.* **71**, 766 (1993).
- [27] H. Kadowaki, K. Motoya, T. J. Sato, J. W. Lynn, J. A. Fernandez-Baca, and J. Kikuchi, *Phys. Rev. Lett.* **101**, 096406 (2008).
- [28] G. Aeppli, W. Bao, C. Broholm, S.-W. Cheong, P. Dai, S. Hayden, T. Mason, H. Mook, T. Perring, *et al.*, in *Spectroscopy of Mott Insulators and Correlated Metals* (Springer, 1995) pp. 205–212.
- [29] W. Bao, C. Broholm, G. Aeppli, P. Dai, J. M. Honig, and P. Metcalf, *Phys. Rev. Lett.* **78**, 507 (1997).
- [30] T. Rice, in *Spectroscopy of Mott Insulators and Correlated Metals* (Springer, 1995) pp. 221–229.
- [31] Y. Q. Li, M. Ma, D. N. Shi, and F. C. Zhang, *Phys. Rev. Lett.* **81**, 3527 (1998).
- [32] K. I. Kugel, D. I. Khomskii, A. O. Sboychakov, and S. V. Streltsov, *Phys. Rev. B* **91**, 155125 (2015).
- [33] A. Joshi, M. Ma, F. Mila, D. N. Shi, and F. C. Zhang, *Phys. Rev. B* **60**, 6584 (1999).
- [34] L. Paolasini, C. Vettier, F. de Bergevin, F. Yakhov, D. Mannix, A. Stunault, W. Neubeck, M. Altarelli, M. Fabrizio, P. A. Metcalf, and J. M. Honig, *Phys. Rev. Lett.* **82**, 4719 (1999).
- [35] M. Fabrizio, M. Altarelli, and M. Benfatto, *Phys. Rev. Lett.* **80**, 3400 (1998).
- [36] S. Di Matteo, N. B. Perkins, and C. R. Natoli, *Phys. Rev. B* **65**, 054413 (2002).
- [37] J.-H. Park, L. H. Tjeng, A. Tanaka, J. W. Allen, C. T. Chen, P. Metcalf, J. M. Honig, F. M. F. de Groot, and G. A. Sawatzky, *Phys. Rev. B* **61**, 11506 (2000).
- [38] S. Y. Ezhov, V. I. Anisimov, D. I. Khomskii, and G. A. Sawatzky, *Phys. Rev. Lett.* **83**, 4136 (1999).
- [39] K. Held, G. Keller, V. Eyert, D. Vollhardt, and V. I. Anisimov, *Phys. Rev. Lett.* **86**, 5345 (2001).
- [40] P. Hansmann, A. Toschi, G. Sangiovanni, T. Saha-Dasgupta, S. Lupi, M. Marsi, and K. Held, *physica status solidi (b)* **250**, 1251 (2013).
- [41] D. Grieger and F. Lechermann, *Phys. Rev. B* **90**, 115115 (2014).
- [42] X. Deng, A. Sternbach, K. Haule, D. N. Basov, and G. Kotliar, *Phys. Rev. Lett.* **113**, 246404 (2014).
- [43] I. Lo Vecchio, J. D. Denlinger, O. Krupin, B. J. Kim, P. A. Metcalf, S. Lupi, J. W. Allen, and A. Lanzara, *Phys. Rev. Lett.* **117**, 166401 (2016).
- [44] F. Mila, R. Shiina, F.-C. Zhang, A. Joshi, M. Ma, V. Anisimov, and T. M. Rice, *Phys. Rev. Lett.* **85**, 1714 (2000).
- [45] R. Shiina, F. Mila, F.-C. Zhang, and T. M. Rice, *Phys. Rev. B* **63**, 144422 (2001).
- [46] A. Joshi, M. Ma, and F. C. Zhang, *Phys. Rev. Lett.* **86**, 5743 (2001).
- [47] L. F. Feiner, A. M. Oleś, and J. Zaanen, *Phys. Rev. Lett.* **78**, 2799 (1997).
- [48] R. E. Word, S. A. Werner, W. B. Yelon, J. M. Honig, and S. Shivashankar, *Phys. Rev. B* **23**, 3533 (1981).
- [49] M. Yethiraj, S. A. Werner, W. B. Yelon, and J. M. Honig, *Phys. Rev. B* **36**, 8675 (1987).
- [50] W. Bao, C. Broholm, G. Aeppli, S. A. Carter, P. Dai, T. F. Rosenbaum, J. M. Honig, P. Metcalf, and S. F. Trevino, *Phys. Rev. B* **58**, 12727 (1998).
- [51] J. E. Keem, H. R. Harrison, and S. P. Faile, *American Ceramic Society Bulletin* **56**, 1022 (1977).

- [52] P. D. Dernier and M. Marezio, *Phys. Rev. B* **2**, 3771 (1970).
- [53] A. Jayaraman, D. B. McWhan, J. P. Remeika, and P. D. Dernier, *Phys. Rev. B* **2**, 3751 (1970).
- [54] G. E. Granroth, A. I. Kolesnikov, T. E. Sherline, J. P. Clancy, K. A. Ross, J. P. C. Ruff, B. D. Gaulin, and S. E. Nagler, *Journal of Physics: Conference Series* **251**, 012058 (2010).
- [55] M. B. Stone, J. L. Niedziela, D. L. Abernathy, L. DeBeer-Schmitt, G. Ehlers, O. Garlea, G. E. Granroth, M. Graves-Brook, A. I. Kolesnikov, A. Podlesnyak, and B. Winn, *Review of Scientific Instruments* **85**, 045113 (2014).
- [56] O. Arnold, J.-C. Bilheux, J. Borreguero, A. Buts, S. I. Campbell, L. Chapon, M. Doucet, N. Draper, R. F. Leal, M. Gigg, *et al.*, *Nuclear Instruments and Methods in Physics Research Section A: Accelerators, Spectrometers, Detectors and Associated Equipment* **764**, 156 (2014).
- [57] S. Toth and B. Lake, *Journal of Physics: Condensed Matter* **27**, 166002 (2015).
- [58] P. Rozier, A. Ratuszna, and J. Galy, *Zeitschrift für anorganische und allgemeine Chemie* **628**, 1236 (2002).
- [59] K. Koepernik and H. Eschrig, *Phys. Rev. B* **59**, 1743 (1999).
- [60] J. P. Perdew, K. Burke, and M. Ernzerhof, *Phys. Rev. Lett.* **77**, 3865 (1996).
- [61] H. O. Jeschke, F. Salvat-Pujol, and R. Valentí, *Phys. Rev. B* **88**, 075106 (2013).
- [62] A. Menth and J. P. Remeika, *Phys. Rev. B* **2**, 3756 (1970).
- [63] P. H. Conlon and J. T. Chalker, *Phys. Rev. B* **81**, 224413 (2010).
- [64] H. E. Stanley, *Phys. Rev.* **176**, 718 (1968).
- [65] A. F. Albuquerque, D. Schwandt, B. Hetényi, S. Capponi, M. Mambrini, and A. M. Läuchli, *Phys. Rev. B* **84**, 024406 (2011).
- [66] F. Mezzacapo and M. Boninsegni, *Phys. Rev. B* **85**, 060402 (2012).
- [67] S.-H. Lee, C. Broholm, G. Aeppli, A. P. Ramirez, T. G. Perring, C. J. Carlile, M. Adams, T. J. L. Jones, and B. Hesse, *EPL (Europhysics Letters)* **35**, 127 (1996).
- [68] E. Samuelsen, M. Hutchings, and G. Shirane, *Physica* **48**, 13 (1970).
- [69] M. Matsuura, Y. Endoh, H. Hiraka, K. Yamada, A. S. Mishchenko, N. Nagaosa, and I. V. Solovyev, *Phys. Rev. B* **68**, 094409 (2003).
- [70] H.-S. Kim, J. Im, M. J. Han, and H. Jin, *Nature communications* **5**, 3988 (2014).
- [71] M. Y. Jeong, S. H. Chang, B. H. Kim, J.-H. Sim, A. Said, D. Casa, T. Gog, E. Janod, L. Cario, S. Yunoki, *et al.*, *Nature Communications* **8**, 782 (2017).
- [72] M. Kresch, M. Lucas, O. Delaire, J. Y. Y. Lin, and B. Fultz, *Phys. Rev. B* **77**, 024301 (2008).
- [73] E. R. Ylvisaker, W. E. Pickett, and K. Koepernik, *Phys. Rev. B* **79**, 035103 (2009).
- [74] T. Mizokawa and A. Fujimori, *Phys. Rev. B* **54**, 5368 (1996).
- [75] J. Y. Lin, H. L. Smith, G. E. Granroth, D. L. Abernathy, M. D. Lumsden, B. Winn, A. A. Aczel, M. Aivazis, and B. Fultz, *Nuclear Instruments and Methods in Physics Research Section A: Accelerators, Spectrometers, Detectors and Associated Equipment* **810**, 86 (2016).